D1

Studies on the nervous control of blood vessels in the anaesthetised rat

Michael P. Gilbey, Dawn R. Collins and Chunhua Huang

Department of Physiology, University College London, London NW3 2PF UK

This work was supported by The Wellcome Trust and the British Heart Foundation.

All procedures accord with current UK legislation.

D2

Developments in morphological and immunohistochemical methods to study physiologically and pharmacologically characterised brainstem neurones

Gareth A. Jones, Ida J. Llewellyn-Smith* and David Jordan

*Department of Physiology, Royal Free & University College Medical School, Rowland Hill Street, London NW3 2PF and *Cardiovascular Neuroscience Group, Centre for Neuroscience, Flinders University, Adelaide, South Australia*

All procedures accord with current UK legislation.

D3

Model studies of arterial, arterial bypass graft and larger bronchial airway flow

C.G. Caro*, N.V. Watkins*, R. Pitt† and S.J. Sherwin†

*Departments of *Bioengineering and †Aeronautics, Imperial College, London SW7 2AZ, UK*

Flow in arteries, arterial bypass grafts and larger bronchial airways can influence local biology/pathology, and conduit geometry may be non-planar (Caro *et al.* 1996, 2002; Sherwin *et al.* 2002). Characteristics of non-planar flows include swirling, bulk mixing and a relatively uniform distribution of wall shear. We report model studies undertaken to clarify the determinants and implications of these flows.

The model comprised effectively two sequential planar bends. ϕ defined the relative rotation of the planes of curvature of the upstream and downstream bends (ϕ = 0 deg co-planar). θ_1 and θ_2 defined the angles subtending the upstream and downstream bends, respectively. We employed a 2-generation bifurcating-tube model (Fig. 1) where the time course of reddening of a litmus coating represented local relative wall shear rate (Caro *et al.* 2002) or a T-tube model with upstream bend (Fig. 2) and CFD (Sherwin *et al.* 1996). The flows were steady, laminar (Reynolds number >> 1) and developed at the inlet.

With ϕ = 90 deg, flow at the downstream bend was swirling with pitch, λ. λ increased downstream of the downstream bend, requiring its measurement at a consistent location. Increase of Re reduced λ, implying Re-dependent biasing of the flow at the upstream bend (e.g. McConalogue & Srivastra, 1968). Change of bend curvature also changes flow biasing (e.g. Agrawal *et al.* 1978). Swirling (and associated phenomena) at the downstream bend largely depend therefore on a Dean-like number at the upstream bend (Dean number (De) = $\mathrm{Re}\,(a/R)^{1/2}$ where a and R are respectively tube radius and radius of curvature). Biasing will attenuate downstream of the upstream bend.

ϕ and θ_2 also influence downstream bend flow. Where ϕ = 0 deg, there is no swirl and increase of Re increases wall shear non-uniformity. Where ϕ > 0 deg, increase of Re increases wall shear uniformity. Where ϕ = 90 deg, λ is minimal and swirl rate, ω, is maximal (since $\lambda = U/\omega$, where U is mean velocity). Increase of θ_2 reduces λ; where θ_2 = 90 deg, λ is least (ω maximal).

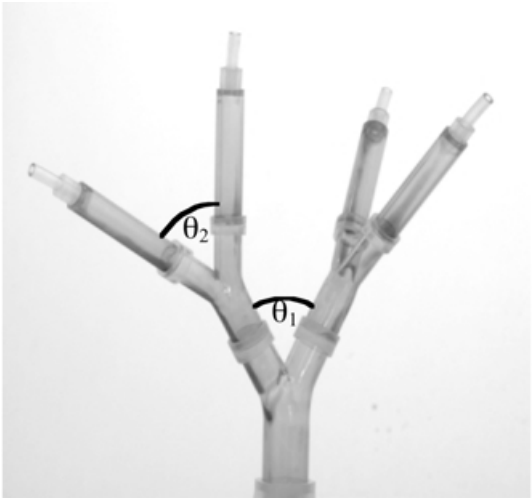

Figure 1.

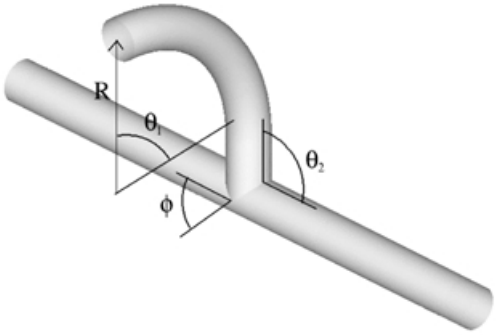

Figure 2.

Atherosclerosis and intimal hyperplasia at arterial bypass grafts develop preferentially where wall shear is low. The findings may be relevant to inhibition of atherosclerosis by exercise and the better prognosis for arterial bypass grafts where 'run off' is high. Swirl will influence inhaled particle/aerosol distribution and flow/airway wall interaction (Lazarowski & Boucher, 2001). Reynolds number dependent λ is consistent with movement of stagnation regions during breathing and cardiac cycles.

Agrawal Y *et al.* (1978). *J Fluid Mech* **85**, 497–518.

Caro CG *et al.* (1996). *Proc Roy Soc* A **452**, 185–197.

Caro CG *et al.* (2002). *Proc Roy Soc* A **458**, 791–809.

Lazarowski ER & Boucher RC (2001). *News Physiol Sci* **16**, 1–5.

McConalogue DJ & Srivastava RS (1968). *Proc Roy Soc* A **307**, 37–53.

Sherwin SJ & Karniadakis GE (1996). *J Comp Phys* **124**, 14–45.

Sherwin SJ *et al.* (2002). *Fourth World Congress of Biomechanics*, Calgary, Aug 4–9, G-209.

D5

Simultaneous confocal imaging of mitochondrial redox state and calcium oscillations at fertilisation or in response to photolysis of caged inositol 1,4,5-trisphosphate in mouse oocytes

Remi Dumollard, Petros Marangos, John Carroll and Michael Duchen

Department of Physiology, University College London, Gower Street, London WC1E 6BT, UK

The accumulation of calcium into mitochondria during cellular calcium signalling represents a primary mechanism that regulates mitochondrial oxidative phosphorylation in response to the increased energy requirements of the cell so often associated with calcium signals. Furthermore, mitochondria may act as spatial buffers for calcium, and so alter the spatiotemporal patterning of calcium signals. In the oocyte, fertilisation triggers stereotypical patterns of calcium waves and oscillations upon which development of the early embryo depends. We have therefore sought evidence to define the influence of the calcium signals on mitochondrial energetics in the mammalian oocyte. This has required the simultaneous measurement and manipulation of $[Ca^{2+}]_c$ together with an assessment of mitochondrial redox state, an index of mitochondrial respiration and activity of the TCA cycle.

Oocytes are recovered from humanely killed MF1 mice as previously described (Halet *et al.* 2002). The isolated oocytes are mounted on a heated stage on a Zeiss 510 CLSM. Changes in $[Ca^{2+}]_c$ following fertilisation are measured using either rhod-2 or fura-red, loaded as the AM esters. Changes in mitochondrial function are measured as changes in NADH (ex. 351 nm, em. 405–485 nm) and/or flavoprotein autofluorescence (ex. 458 nm, em. > 505 nm), measured sequentially using the 'multitracking' facility of the Zeiss CLSM. We have in these experiments routinely seen oscillations in mitochondrial autofluorescence closely associated in time with $[Ca^{2+}]_c$ transients, strongly suggesting that $[Ca^{2+}]_c$ signals are transmitted to mitochondria and modulate mitochondrial metabolism. We will demonstrate a protocol for the simultaneous measurement of flavoprotein and NADH autofluorescence with $[Ca^{2+}]_c$, together with the photolysis of caged $InsP_3$ or fertilisation to initiate $[Ca^{2+}]_c$ oscillations.

Halet G *et al.* (2002). *J Cell Sci* **115**, 2139–2149.

R.D. is supported by a Marie Curie Fellowship. J.C. and M.D. are funded by grants from the MRC and The Wellcome Trust.

All procedures accord with current UK legislation.

D6

A simple 'Q box' for an atomic force microscope

Jenny Clark and Jonathan F. Ashmore

Department of Physiology and UCL Centre for Auditory Research, University College London, Gower Street, London WC1E 6BT, UK

Atomic force microscopy (AFM) is a technique that allows surface topography of structures to be measured with, in principle, sub-nanometre resolution. Various modes of using the microscope are popular. In contact mode, the surface is scanned with the AFM cantilever in continuous contact so as to maintain a constant force between the lever tip and the surface. In non-contact modes, the scanning may involve only intermittent contact during the extreme of a rapid oscillatory excursion of the tip. It is generally thought that such non-contact modes may be more suitable for imaging soft biological samples since the current microfabrication techniques produce cantilevers that are quite stiff (commercially available levers have tip stiffness greater than 0.01 N/m). In biological contexts and in solution, all motions of the cantilevers are severely damped. The resonant excursions of microlevers thus provide less effective information about surface structures, and contact modes are used in preference. To overcome this problem we have followed an evolutionary solution found in the mammalian cochlea to use positive feedback to cancel viscous damping of the oscillating cantilever (Tamayo *et al.* 2001).

The demonstration is based around a commercially available AFM ('Nomad', Quesant Instrument Corp., CA, USA). The circuitry and software of this AFM can be conveniently modified. The AFM has an open architecture that allows access for patch pipettes to record from cells while they are being scanned. The design is such that the cantilever is driven into resonance by means of a small piezoelectric element mounted close to the cantilever and which is secondary to the XYZ piezoelectric scanning elements. We have built an ancillary electronic circuit (or 'Q box') that modifies the quality factor of the cantilever resonance. The circuit works by using the position signal of the cantilever (detected by a photodiode as part of the AFM control circuitry) and feeding the signal back with gain and appropriate phase to enhance the resonance. The circuit uses a small number of components and can easily be added to one of the Quesant circuit boards. The 'Q-box' is implemented in hardware as the resonant frequencies of some cantilevers can exceed 40 kHz.

Although similar modifications are now beginning to be provided as (costly) add-ons to commercial AFMs, the 'Q box' we have designed is instructive and provides insight into the complex dynamics of nanoscale structures. The demonstration will show examples of the biological sample images obtained, as well as progress towards designing an optimal scanning head for studying patch-clamped hair cells.

Tamayo J *et al.* (2001). *Biophys J* **81**, 526–537.

This work was supported by The Wellcome Trust. J.C. held a Physiological Society Vacation Studentship.

All procedures accord with current UK legislation.

D7

Inner and outer hair cell endocytosis studied by two photon laser scanning confocal microscopy

C.B. Griesinger, C.D. Richards and J.F. Ashmore

Department of Physiology, University College London, Gower Street, London WC1E 6BT, UK

Cochlear hair cells show pronounced endocytosis from their apical surface (Meyer *et al.* 2001; Griesinger *et al.* 2002). To assess the role of apical endocytosis, we used two-photon imaging of fluorescent markers to study endocytosis and protein uptake in hair cells in the *in situ* epithelium of adult guinea-pigs, killed by quick cervical dislocation in accordance with UK legislation.

Both inner and outer hair cells (IHCs and OHCs) showed rapid calcium-dependent internalisation of apical FM 1–43 (5 μM)-labelled membrane. The delay between signal in plasma membrane and that in internal endosomes was similar for IHCs (20 s) and OHCs (25 s). Both calcium dependency and fast rate

suggest the presence of clathrin-independent endocytosis. Disruption of mechanotransduction did not change FM 1–43 uptake. Hence all internal signal was derived from endocytosis. In both cells, the fluid phase marker Lucifer Yellow (20 mM) revealed staining patterns similar to that of FM 1–43. Both IHCs and OHCs showed a functional domain dedicated to membrane internalisation at their apical membrane. IHCs internalised membrane from a ring around the cuticular plate, while OHCs showed membrane uptake from a circular patch within the cuticular plate.

IHCs and OHCs differed in patterns and kinetics of membrane trafficking. IHCs showed rapid kinesin-dependent trafficking of apically internalised membrane to about 30 basolateral hotspots at the synaptic pole. These reached 60 % of the intensity of the apical signal. In contrast, OHCs showed only weak labelling (5 % intensity compared with apex) of a disk-like structure (about 8 μm diameter) at the synaptic pole, most likely the basal cisterna. Instead, OHCs showed rapid kinesin-independent trafficking of membrane to patches along the basolateral membrane that showed strong signal (90 % of apical signal) and subsequently (66 s later) to a central strand.

To test an involvement of apical endocytosis in protein recycling, we used FITC-labelled lectin wheatgerm agglutinin (WGA), a marker for adsorptive endocytosis. WGA labels proteins containing *N*-acetyl-glucosamine, a signal for apical protein sorting in epithelial cells. Only OHCs internalised WGA through small vesicles about 1 μm in diameter in the apex. WGA appeared in the apical part of the basolateral membrane after a delay of about 50 min. Thus OHCs feature the 'indirect route' of protein uptake by transcytosis, described for various epithelial cells. However, at the apical membrane WGA signal was excluded from the domain dedicated to membrane uptake. The data suggest that there are spatially distinct pathways for protein and membrane trafficking in OHCs.

Griesinger CB (2002). *J Neurosci* **22**, 3939–3952.

Meyer J *et al.* (2001). *Hear Res* **161**, 10–22.

This work was supported by the MRC, Wellcome Trust and BBSRC.

All procedures accord with current UK legislation.

D8

A method for measuring longitudinal nerve and tendon movement from high-frequency ultrasound images

Andrew Dilley and Bruce Lynn

Department of Physiology, University College London, London WC1E 6BT, UK

During limb movement nerves have to slide and stretch, but the extent of such nerve movements has not been accurately assessed *in vivo*. This is a question of possible clinical interest since nerve entrapment syndromes, where such sliding may be altered, are common and present a significant health problem.

A method to measure transverse nerve movement from ultrasound images by measuring the distance between the nerve border and fixed structures was developed previously (Lynn *et al.* 2001). Since nerves are continuous structures, it is not possible to measure longitudinal movement in this way. To study nerve sliding *in vivo*, a non-invasive method was required. Doppler ultrasound can detect nerve movements (Hough *et al.* 2000), but the velocity of nerve sliding is at the lower limit of the method. Using frame-by-frame cross-correlation analysis of high-frequency ultrasound images, we have developed a method to measure longitudinal movement of peripheral nerves (Dilley *et al.* 2001).

Sequences of ultrasound images are captured at 10 frames s^{-1} using a Diasus ultrasound system (Dynamic Imaging, UK) with a 10–22 MHz, 26 mm linear array transducer and analysed off-line using software developed in Matlab (Mathworks, USA). Resolution of the images is 0.093 mm $pixel^{-1}$ and image size was 280 × 440 pixels. The analysis software employs cross-correlation to determine relative movement between adjacent frames in sequences of ultrasound images. The programme calculates the correlation coefficient between the pixel grey levels for selected regions of tissue in two adjacent images. In the compared frame, the co-ordinates of the region of interest are offset along the horizontal image plane by a pixel at a time within a predetermined range (typically ± 15 pixels, i.e. ± 1.35 mm). The correlation coefficient is calculated for each individual pixel shift and the cross-correlogram is plotted. The region of interest is also offset along the vertical image plane (± 2 pixels) to compensate for any small vertical movements of the nerve. At each vertical offset a cross-correlogram is plotted in the horizontal image plane. A quadratic equation fitted to the maximum coefficient and its two adjacent values in each correlogram allows the estimation of the pixel shift to sub-pixel precision. The peak correlation coefficient in the two planes is used to estimate the shift in region of interest between frames. The program calculates the relative movement for each pair of adjacent frames in ultrasound sequences. The frame interval is increased to improve the accuracy of the correlation algorithm at low velocities (< 2 pixels). Best values are assessed from consistency of pixel shifts at different frame intervals and the *a* coefficient of the quadratic equation that defines the narrowness of the peak in the cross-corellogram.

Preliminary *in vitro* measurements on phantoms gave accurate estimates for movements, and reliable results were also obtained when the transducer was moved over the surface of the forearm at constant velocity.

Median nerve sliding has been examined during a range of limb movements in subjects and patients in studies approved by the local ethical committee. For example, sliding of the median nerve in the forearm and upper arm was determined during 40 deg wrist extension in 11 control subjects. The mean nerve movement in the forearm was 4.1 ± 0.94 mm (mean ± S.D.) and upper arm 1.7 ± 0.55 mm with the arm in 90 deg shoulder abduction. These results were consistent with nerve sliding estimates on cadavers and also expected values based on the anatomy of the wrist. Estimates of additional nerve strain were determined from measurements at different locations and indicated an additional strain of 1.1 % on the median nerve in the proximal forearm following 40 deg wrist extension. Movement of flexor digitorum profundus was also examined in seven subjects during 30 deg extension of the index finger from full flexion. Mean excursion in the distal forearm was 14.2 ± 4.4 mm.

In summary, the present method can be used to reliably measure longitudinal sliding from high-frequency ultrasound images of peripheral nerves, as well as other soft tissues (e.g. tendon, muscle). This method is currently being used to investigate altered nerve sliding in patients with nerve entrapment.

Dilley A *et al.* (2001). *Ultrasound Med Biol* **27**, 1211–1218.

Hough AD *et al.* (2000). *J Hand Surg* **25B**, 585–589.

Lynn B *et al.* (2000). *J Physiol* **523.P**, 136*P*.

This work was supported by the Arthritis Research Campaign.

All procedures accord with current local guidelines and the Declaration of Helsinki.

D9

Digital spike discrimination combining size and shape elements

R.E.J. Dyball and G.S. Bhumbra

Department of Anatomy, University of Cambridge, Cambridge CB2 3DY, UK

Accurate discrimination of spike activity from extracellular recordings is very important when analysing neural activity. Analogue hardware discrimination is commonly used because of its speed and ease of use. However, such methods usually rely on 'window discrimination' that is dependent on the size of spikes compared with the background noise. Similar techniques are available in software packages that employ digital discrimination. However, both hardware and software are liable to miss spikes and count artifact events as biological spikes.

The methods proposed here combine the intuitive nature of oscilloscope window discrimination with digital shape evaluation. The first stage mimics a level discriminator: an initial trigger level set very close to the noise level is used to extract potential spikes and generous window discrimination can be used to exclude very large artifacts such as those of a stimulus. The second stage plots the real and imaginary coefficients of the fast Fourier transform of specifiable orders, for a user-selected region of potential spike shapes. Other parameters of shape, such as the maximum gradient or a cursor value at a given time reference, may also be plotted.

Event inclusion is specified by a graphical user interface based on set theory. A user-modifiable elliptical function can be used to include or exclude scatter points of three two-dimensional plots of customisable shape parameters. An intuitive colour-coded interface employs Boolean logic to enable the user to specify which subsets represent genuine spikes. To assist each decision, a waveform overlay is given and an inter-spike interval histogram is shown to highlight short intervals and missing spikes. The logical interface allows the user to review rapidly all those wave sections, possibly considered as artifacts, that were not counted as spikes. Prior to acceptance, the user is invited to review the whole waveform record with the discriminated extracts displayed alongside.

Missed spikes give inappropriately long intervals whereas artifacts counted as spikes can manifest as very short intervals. Accurate discrimination is essential when analysing inter-spike intervals rather than mean spike frequency. It is particularly important when attempting to distinguish different cells recorded simultaneously from the same electrode.

This work was supported by Merck, Sharp and Dohme, and the James Baird Fund.